Astron. Astrophys. 331, 934–948 (1998)

ASTRONOMY AND ASTROPHYSICS

The new Basel high-latitude field star survey of the Galaxy

I. General introduction, methodology and first analysis

Roland Buser[1], **Jianxiang Rong**[2], **and Salih Karaali**[3]

[1] Astronomisches Institut der Universität Basel, Venusstr. 7, CH-4102 Binningen, Switzerland
[2] Astronomy Department, Nanjing University, Nanjing 210008, P.R. China
[3] Istanbul University Science Faculty, Department of Astronomy and Space Sciences, TR-34452 University - Istanbul, Turkey

Received 1 August 1997 / Accepted 10 November 1997

Abstract. This is the first in a series of papers devoted to the determination of Galactic structure from the new homogeneous catalog of photographic RGU field star data in fourteen high-latitude directions. We give a general description of the motivation for this work, the construction of the observational data base, and the structural Galaxy models designed for its analysis. In particular, we provide a concise yet comprehensive account of the statistical methodology used for determining reliable constraints to the model parameters. Preliminary results obtained from the first-half sample of seven fields are discussed to demonstrate the significance of the approach.

Our best models suggest that the *thick disk* component has a local density of $5.4 \pm 1.5\%$ relative to the thin disk, an exponential scale height of 1.15 ± 0.15 kpc, and mean metallicity $\langle [M/H] \rangle \sim -0.6$ dex with dispersion $\sigma_{\langle [M/H] \rangle} \sim 0.4$ dex. However, because the present data cannot exclude the existence of a vertical metallicity gradient $\partial [M/H]/\partial z \sim -0.10 \pm 0.10$ dex/kpc, a sharper picture of the thick disk metallicity structure must await the analysis of the full–survey data in 14 fields.

Key words: Galaxy: abundances – Galaxy: general – Galaxy: stellar content – Galaxy: structure

1. History and introduction

The Basel Palomar–Schmidt RGU–photographic survey has been a major project that pioneered the study of the Galactic field halo when it was begun in the mid–sixties (Becker 1965). With the growth of the plate material obtained in an increasing number of fields, the following two decades saw the gradual emergence of a large–scale halo component whose significantly flattened density distribution was in sharp contrast to the essentially spherical halo occupied by the globular clusters (Becker 1980, Buser & Kaeser 1985). However concurrently, new photometric, spectroscopic, and proper motion surveys accumulated increasing independent evidence of a *thick disk* population component with a density gradient that appeared to be similarly intermediate between the *thin disk* and the *conventional spheroid* as was observed in the Basel *halo* data (e.g., Reid & Gilmore 1982). Indeed, Bahcall et al. (1985) and Fenkart (1989a–d) subsequently showed that the Basel RGU high–latitude survey data could also be described with a model containing a thick disk component having a local density of 2 percent and a scale height of order 1 kpc. It thus became evident that, since the Basel RGU survey penetrates to faint enough magnitudes ($m_G \approx 19$ or $m_V \approx 18$) for a significant sampling of this intermediate population component, advantage must be taken of its unique properties of providing three–color data – including the metallicity–sensitive $U-G$ colors – *and* systematic directional coverage of a significant number of fields in order to derive **more reliable estimates** of the *larger–scale structural parameters of the density, luminosity, and metallicity distributions of the Galactic thick disk stars* than had been inferred from the previous limited analyses of the original survey data.

This task, however, could not be attempted using the available original catalogs, because detailed investigations of the data in a number of individual fields revealed the existence of inhomogeneities, systematic calibration errors, and color equations that could not be corrected by simple means *a posteriori* but that were shown to be traceable to the lack of an adequate standard of the RGU photometric system (Buser 1988). We thus determined to establish the required standard and calibrations using synthetic photometry techniques, and to construct a new homogeneous data base from the available plate material *ab initio* (Buser & Fenkart 1990).

Construction of the new data base was begun in 1990 and will be completed in 1997. The catalog will be published in Papers III and IV of this series (Buser et al. 1997a,b) and is briefly described in Sect. 2 below. In Sect. 3 we describe the basic model calculations that we have been using to analyse the catalog. The tools and procedures for the analysis are detailed in Sect. 4. A discussion of test results obtained from the first–

Send offprint requests to: Roland Buser

half sample of the data for seven fields is then given in Sect. 5 to demonstrate the feasibility of the present approach. Finally, in the concluding Sect. 6 we give a brief outline of the work covered in the subsequent papers of this series.

2. The new catalog of homogeneous RGU data

As summarized in Table 1, the catalog comprises new photographic three–color data for more than 18,000 stars remeasured with the Iris photometer from the Basel Palomar–Schmidt survey plates in 14 original intermediate– and high–latitude fields. While the original catalog data obtained from the same plates (Becker & Fenkart 1976 (I), Becker et al. 1976 (II), Becker et al. 1978 (V), Becker et al. 1988 (XI), Becker et al. 1989 (XII)) were derived based on a *preliminary standard of the RGU photometric system and methodology* which allowed to pioneer the exploration of the space density distributions of the field–halo stars down to the faintest observed magnitude limits, in the present work we have rather attempted to exploit the *significantly improved calibration and standardization of the RGU photometric system* which have been established in recent years and which allow us to provide *photometric data of high systematic accuracy and homogeneity* – an indispensable requirement for the more ambitious goal of a physically consistent determination of the density *and* the metallicity distributions of the stars. Thus, the following basic principles were adopted for the construction of the present new catalog:

1. All the data have been derived following the *definition and standard of the photographic RGU system* based on synthetic photometry, as summarized in Buser & Fenkart (1990). In particular, calibration of the RGU plates has been done employing *available photoelectric UBV standard sequences* exclusively. From these, equivalent *standard RGU data* were derived via *UBV–RGU transformations* which account for the systematic differences of the stellar spectral energy distributions due to their different physical parameters, such as effective temperatures, luminosities, and metallicities (Buser 1978, 1988; Güngör 1996, Buser et al. 1997c). Thus, the RGU calibration standard magnitudes and colors are comprehensively and consistently tied with the standard UBV data *throughout the observed ranges in physical properties of the stars* – which eliminates the serious limitations of the preliminary RGU standard and its associated systematic errors propagating into the original catalog data (Buser 1988, Buser & Rong 1995).
2. Stars have been included in the catalog only down to the magnitude limits defined by the *available photoelectric UBV standard sequences used for the plate calibrations*. Extrapolations of the characteristic curves were strictly limited to less than about 0.5 magnitudes fainter than the faintest photoelectric data point. In particular, all extensions employing additional independent electronographic and/or photographic data – a method often employed to expand the magnitude ranges in the original catalogs – were deliberately excluded from the calibration process, because in no case did such data allow to reconstruct the corresponding photometric systems with sufficient accuracy and confidence (Buser 1988).
3. *Photometric standardization of the photographic program stars* has been based strictly and uniformly on the evaluation of *color equations* defined by the magnitude residuals (as functions of observed colors) for the calibration standard stars. Because the preliminary RGU standard was ill–defined – or not defined at all – outside its limited color (or physical parameter) range of application, a systematic color correction based on the "final" two–color distributions of the program stars often had to be substituted for this fundamental step as part of the data *interpretation* – implying significant loss of control of the real significance of the data in the original catalogs.
4. As in the original field survey, the probability of *field errors* has been minimized by selecting relatively small–sized fields near the plate centers and standard star sequences. In fact, the usual zonal checks revealed field errors in a few cases only which then were accounted for by standard methods.

While the full details on the error budget in the catalog data will be given in Papers III and IV, it may suffice here to mention that the above procedure applied to an average of 5 plates per color (i.e., a total of 15 plates per field) provides G magnitudes and G-R and U-G colors with typical internal errors of $\sigma_G = 0.05, \sigma_{G-R} = 0.07$, and $\sigma_{U-G} = 0.08$ mag. For each field, the resulting catalog of *star counts as functions of observed apparent magnitude and colors,* $N(G), N(G-R|G)$, *and* $N(U-G|G)$ then constitutes the data base used for testing the interpretive models.

3. Methodology

3.1. Concept

Analysis of the catalog is done essentially following the approach taken by Buser & Kaeser (1985) and summarized by Buser & Fenkart (1990): we adopt a parameterized model of the density distributions, luminosity functions, and color–magnitude relations assumed to represent the various stellar population components of the Galaxy, whence we calculate the expected star counts and color distributions for each field. Systematic variation of parameter values then allows us to evaluate, by least–squares techniques, those models which best fit the observed distributions for each individual field or for a number of fields. Eventually, we determine the most stringent constraints to the model parameters imposed by the all–survey data.

3.2. Models: ingredients

3.2.1. Galactic population components

Our models comprise four distinct population components of luminous stars, as follows: a *thin disk*, which is composed of a *young* and an *old* component, a *thick disk*, and a *halo*. The primary characteristic of each of these components is its *density law*, which we assume to be given by one of the parameterized

Table 1. The new Basel high–latitude Palomar–Schmidt survey field data[1]

	Field	l	b	Area (deg^2)	$m_{G,cat}$	$m_{G,lim}$	E_{G-R}	No. of stars
1	Praesepe	205.9	+32.4	3.56	16.0	15.0	0.00	1228
2	M101	101.0	+60.0	2.00	20.0	18.5	0.00	1388
3	M67	210.6	+32.2	1.70	17.5	16.0	0.00	748
4	SA54	200.1	+58.8	2.56	19.5	18.5	0.00	1359
5	SA57	65.5	+85.5	2.61	19.5	19.0	0.00	1807
6	SA141	245.0	-85.8	1.92	18.5	17.5	0.00	758
7	M5	4.0	+47.0	1.05	19.5	18.5	0.00	1819
	1–7			15.40				9107
8	M67U	215.7	+32.0	3.60	17.0	15.0	0.00	1288
9	SA51	189.2	+20.9	0.45	19.0	18.0	0.00	1131
10	SA71	167.0	-34.0	2.97	20.0	18.0	0.00	2021
11	SA82	6.3	+66.3	1.20	19.0	18.0	0.00	1030
12	SA94	175.3	-49.2	2.03	20.0	17.5	0.00	1187
13	SA107	5.7	+41.3	0.95	17.0	16.5	0.15	532
14	NGC6171	3.3	+22.8	0.92	18.5	18.0	0.45	1970
	8–14			12.12				9159
	1–14			27.52				18266

[1] The catalog of photometric data is being published in Paper III (fields 1–7) and in Paper IV (fields 8–14) of this series.

analytical functions discussed in 3.2.2 and 3.2.3 below. The secondary characteristic of each component is its *luminosity function*, which we assume to be given by the luminosity function derived from observations of the nearby and/or other component tracer stars described in 3.2.4. Finally, since we also want to determine the *chemical signature* of each population component, the characteristic (or template) color–absolute magnitude and two–color diagrams are given as functions of stellar *metallicity*, and are discussed in more detail in subsection 3.2.5 below.

3.2.2. Density laws

The density laws adopted for the disk population components are the usual double–exponentials

$$D_i(x,z) = n_{i,0} e^{-(x-r_0)/d_i} e^{-z/h_i}, \qquad i = 1,2,3,$$

with local densities $n_{i,0}$, scale lengths d_i, and scale heights h_i. For the (spheroidal) halo, we assume a de Vaucouleurs density distribution,

$$D(R) = n_{halo} (R/r_0)^{-7/8} e^{-7.669 R_{eff}^{-1/4}(R^{1/4} - r_0^{1/4})},$$

where n_{halo} is the local density and R_{eff} is the effective radius, and where

$$x = (r_0^2 + r^2 cos^2 b - 2 r_0 r cos l cos b)^{1/2},$$

$$z = r|sin b|,$$

$$R = (x^2 + (z/\kappa_0)^2)^{1/2},$$

κ_0 being the flattening factor of the halo. In the above equations, l and b are the Galactic coordinates, and x and z are the galactocentric cylindrical coordinates of a given point (distance from the Galactic center projected upon the Galactic plane, and height above the Galactic plane, respectively); r is the given point's distance from the sun, and r_0 is the distance of the sun from the Galactic center (assumed to be 8.6 kpc).

3.2.3. Density law parameters

Table 2 gives a summary of the parameter ranges which we adopt for the systematic exploration of parameter space by calculating a large number of models. They are chosen such as to provide fair coverage of published parameter values suggested by modern surveys (cf. Bahcall 1986, Gilmore et al. 1990, Majewski 1993, and Blitz & Teuben 1996 for recent reviews). In the actual calculations, a uniform distribution of between four and eight discrete values are employed to cover the range for each parameter. According to the different anticipated (or supposed) sensitivities of the present survey data to variations of the different parameters, the latter are divided into primary and secondary categories: the majority of *primary* parameters are expected to be well determined from the present data, while the majority of *secondary* parameters are expected to provide indispensable but only less–well determined constraints to the models.

3.2.4. Luminosity functions

We have used two basic luminosity functions (LFs) to define the appropriate input data for the different population components: (1) the LF derived by Buser & Kaeser (1985) from the Gliese (1969) nearby star catalog, and (2) the LF derived by Da Costa (1982) for the globular cluster 47 Tuc. Note that the Buser & Kaeser LF was derived for star systems rather than for individual stars, counting all the components of a binary or multiple system with separations $\leq$ 100" as a single object of combined absolute magnitude. This selection thus refers to those Gliese systems which are unresolved on the Palomar–Schmidt plates if observed at distances $\geq 1 kpc$, as is appropriate for the majority of the present survey field stars. This accounts for the low value of $0.08 stars/pc^3$ for the local density of old thin disk dwarfs (i.e., systems), as opposed to the corresponding $0.11 stars/pc^3$

Table 2. Variation ranges of density law parameters

Component		Parameter	Category[1]	Symbol	Unit	Range adopted
Thin disk		local density	II	n_0	stars pc^{-3}	0.070 – 0.100
	old	scale length	I	d_1	kpc	2.5 – 5.5
		scale height dwarfs	I	h_1	325 pc	0.8 – 1.2
		scale height giants	II	h_2	kpc	0.15 – 0.35
	young	scale length	II	d_2	kpc	3.0 – 4.5
		scale height	I	h_3	kpc	0.10 – 0.25
Thick disk		local density	I	n_1	n_0	0.00 – 0.09
		scale length	II	d_3	kpc	3.5 – 5.0
		scale height	I	h_4	kpc	0.9 – 1.5
Halo		local density	I	n_2	n_0	0.0000 – 0.0025
		effective radius	II	R_{eff}	kpc	2.1 – 3.3
		flattening	II	κ_0	–	0.7 – 1.0

[1] The parameters are divided into *primary* (I) and *secondary* (II) categories, according to the hierarchy of the computational steps.

obtained for the single-star LF by Wielen et al. (1983). Thus, for the thin-disk dwarfs and giants, we have used the LFs given in Buser & Kaeser (1985).

For the thick-disk and halo stars, we adopted the following LFs. For magnitudes $M_V \leq 5$, the shape of the LF is given by the 47 Tuc LF of Da Costa (1982), while for the fainter stars, the shape given by the old thin-disk LF of Wielen et al. was joined smoothly with the brighter LF at $M_V = 5$. Thus, while we assume the thick-disk and halo LFs to have the same shapes, their local normalizations relative to the thin disk were left as independent parameters – to be determined by the present analysis of the new Basel survey data.

Thus in this paper, we adopt a unique LF for each individual component, which we also assume to be the same throughout the range of the survey, and which are illustrated in Fig. 1. Effects of canonical uncertainties and intrinsic errors in the adopted LFs have been shown to be of minor importance in the analysis of the original star count and color survey data (Buser & Kaeser 1985), and are confirmed here. Later on (in Paper II), we shall relax the constraint of uniqueness by examining a number of alternatives. Eventually, we shall introduce analytical luminosity functions derived from mass functions and evolutionary calculations in order to explore the sensitivity of photometric star count and color surveys on luminosity function variations more deeply – with an eye on the important question of age–dating the population components.

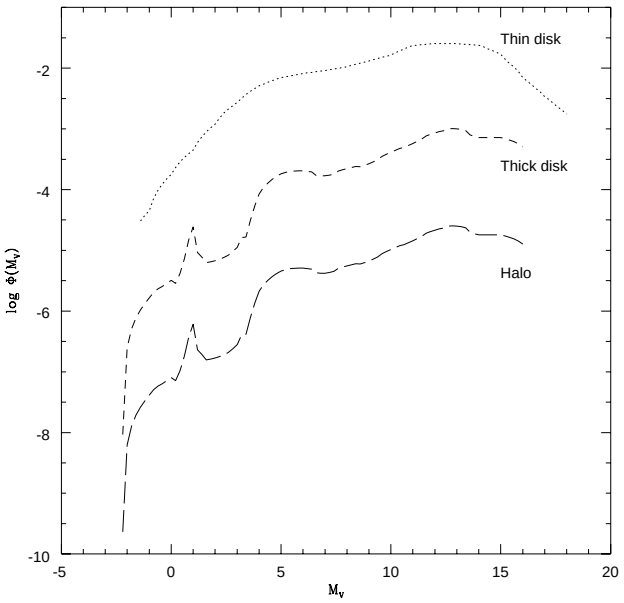

Fig. 1. Luminosity functions for the different population components, with adopted local densities $n_0 : n_1 : n_2 = 1 : 0.04 : 0.001$.

3.2.5. Color–magnitude and two–color relations, and transformations from UBV to RGU

For the calculation of star counts as functions of apparent magnitude and colors, the above luminosity functions – which are given in the UBV–standard system of the absolute M_V-magnitudes – were converted to functions $\Phi_i[M_V, (B-V)_0]$ by using the intrinsic color–absolute magnitude diagrams derived from observations of tracer stars for the chemically different population components. For the thin–disk solar–abundance dwarfs, we have adopted the relation established by Buser & Fenkart (1990), which in turn was based on the compilations published by Schmidt–Kaler (1965, 1982), Gliese (1982), and Jahreiss & Gliese (1989), while for the thin–disk (solar–abundance) giants we used Table 2 given by Buser & Kaeser (1985), which was derived from the Gliese (1969) catalog and which was found to be very similar to the semi–empirical relation obtained by Neckel (1975) from a large sample of giants with spectroscopic parallaxes. On the other hand, the lower–abundance stars of the thick disk and halo have been represented by Sandage's (1982) template color–absolute magnitude diagrams for the globular clusters 47 Tuc, M5, and M92, whose metallicities were adopted to be $\langle[M/H]\rangle = -0.85, -1.31$ and -2.05, respectively (Pilachowski 1984).

Finally, the resulting $\Phi_i[M_V, (B-V)_0]$ were combined with the appropriate metallicity–dependent $(U-B)_0$ vs. $(B-V)_0$ color–color relations constructed from extant data by Johnson (1966), FitzGerald (1970), Carney (1979), Arimoto (1986),

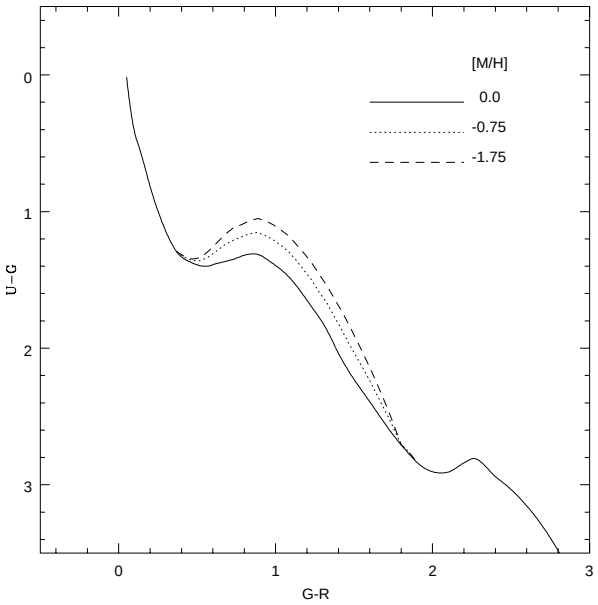

Fig. 2. The RGU two–color diagram for dwarf stars of different metallicities, as transformed from the corresponding UBV diagram.

and Yoshii et al.(1987), whence detailed luminosity functions, $\Phi_i[M_G,(G-R)_0]$ and $\Phi_i[M_G,(U-G)_0]$, have been derived for both dwarfs and giants covering the metallicity range $0.0 \geq \langle[M/H]\rangle \geq -2.0$ *via* the corresponding transformation equations based on synthetic UBV and RGU photometry (Buser & Fenkart 1990, Buser & Kurucz 1992, Güngör 1996, Buser et al. 1997c).

A sample two–color diagram which results from the transformation and interpolation processes applied to the UBV data for dwarfs is shown in Fig. 2; also note that the component–specific luminosity functions calculated above provide the final input in the star–count Eq. (1) below.

3.2.6. Interstellar reddening and extinction

As shown in Table 1, significant interstellar reddening has been measured from the two–color diagrams in only two fields, SA107 and NGC6171, which belong to the inner halo/bulge part of the survey and which will be analysed including appropriate modelling in Paper V of this series. Zero reddenings are also deduced from the maps of Burstein & Heiles (1982) for six out of the fourteen Basel fields; for the remaining eight directions, this same source gives $E_{B-V} \leq 0.1$ mag, which translates to $E_{G-R} \leq 0.13$ mag. While these minor interstellar reddening values would not change the conclusions of the present paper, we prefer the values of Table 1 since they are specific for the small areas investigated here.

3.3. Models: general outline of calculations

Of course, the purpose of this project is to determine those specific characteristics of the Galactic population components whose combination provides both a physically plausible picture *and* the best possible consistency with the observed survey data, $N(G, G-R, U-G)$, where N is the number of stars counted as a function of apparent G–magnitude and/or $G-R$ and/or $U-G$ color. Thus, simulated star counts and color distributions are calculated from a Galactic model specified by a set of parameter values selected from the ranges adopted in Table 2. Variation of parameter values then leads to a large number of models providing full coverage and allowing a systematic exploration of the adopted parameter space.

In rough outline, the sequence of calculations is as follows:

1. Initially, we assume the (mean) *metallicity* of each component to be fixed at $\langle[M/H]\rangle$ = $(0.00, -0.75, -1.75)dex$ for the old and young thin disks, the thick disk, and the halo, respectively.
2. Adopting a fixed value for each of the secondary parameters, models are calculated for all combinations of primary parameter values covering the full ranges adopted in Table 2. Results are then used to derive *optimum primary parameter values and constraints* by comparison with the observed *two–color (G, G-R) data* and doing the statistical analysis detailed in Sect. 4.
3. Keeping the optimum primary parameter values fixed, models are calculated for all combinations of secondary parameter values covering the full ranges adopted in Table 2. Results are then used to derive *optimum secondary parameter values and constraints* in the same way as for the primary parameters before.
4. A second iteration between steps (2) and (3) is performed to establish convergence toward stable results – which turns out to be achievable without further iterations in most cases. Thus, for each iteration a total of nearly 17,000 models are calculated for the systematic determination of optimum parameter values and constraints for both individual fields and the all–field survey.
5. Adopting the above optimum values and constraints for the full dozen of primary and secondary (structural) parameters, new models are then calculated for ranges of mean metallicities and metallicity gradients of the Galactic population components, whence *optimized values for the mean metallicities and metallicity gradients* are derived by comparison with the observed *three–color (G, G-R, U-G)* data and doing a similar statistical analysis as before.
6. Finally, a second iteration through the full sequence of calculations is performed by propagating the improved values for the mean metallicities from step 1 through step 5.

3.4. Models: basic calculations

For each model, the basic calculation provides *differential* star counts (i.e., for the apparent magnitude interval $m_1 \leq m < m_2$ and the color index interval $c_1 \leq c < c_2$) for a field subtending solid angle ω in Galactic direction l, b, according to the fundamental equation of stellar statistics:

$$N(m_1, m_2, c_1, c_2, l, b, \omega) = \sum_{i=1}^{4} N_i(m_1, m_2, c_1, c_2, l, b, \omega) =$$

$$\sum_{i=1}^{4} \omega \left[\int_{m_1}^{m_2} \int_{c_1}^{c_2} \int_{0}^{r_c} r^2 \cdot D_i(r) \cdot \Phi_i(M,c) \cdot dr \cdot dc \cdot dm \right], \quad (1)$$

where D_i and Φ_i are given by the component–specific density laws and luminosity functions, respectively, and

$$M = m - 5logr - A(r) + 5$$

is the absolute magnitude of the star, $A(r)$ is the total Galactic extinction along the line of sight out to distance r from the sun, and r_c is the integration cutoff.

4. Comparison with observations and analysis

4.1. χ^2*–calculations*

In order to compare calculations and observations for a given field k, both model–generated and observed data are first sampled into apparent magnitude and color bins of sizes 0.5 mag and 0.2 mag, respectively. From these, the (computed or observed) *star counts per square degree*, $N(G)$, $N(G-R)$, $N(U-G)$, $N(G,G-R)$, $N(G,U-G)$, falling into successive apparent magnitude or/and color bins are established, and for each model, χ^2–estimates of goodness–of–fit to the observed one– or two–dimensional distributions are then calculated as follows:

$$\chi^2_{1,k} = \sum_{bins} [N_{obs}(G,G-R) - N_{mod}(G,G-R)]^2,$$

$$\chi^2_{2,k} = \sum_{bins} [N_{obs}(G) - N_{mod}(G)]^2,$$

$$\chi^2_{3,k} = \sum_{bins} [N_{obs}(G-R) - N_{mod}(G-R)]^2,$$

where the field index $k = 1, \ldots, 7$.

For each field k, the *individually best–fitting model* is determined by its lowest–$\chi^2_{1,k}$ value, $\chi^2_{1,k,min}$, while measures of each model's *simultaneous fitting to the combined all–survey data in seven fields* are thus given by the global χ^2–values

$$\chi^2_{i,s} = \sum_{k=1}^{7} \chi^2_{i,k}/7, \qquad i = 1,2,3,$$

whence the *globally best–fitting model* is identified by the lowest–$\chi^2_{1,s}$ value, $\chi^2_{1,s,min}$.

The (seven) individually plus the (one) globally best–fitting models are used as pivots in the subsequent analyses.

4.2. Determination of optimized parameter values

Using the above results for a total of nearly 17,000 models for each of 7 fields plus their combination, we now determine the optimized values for each of the 12 primary and secondary parameters.

4.2.1. χ^2–curves

For each parameter, we determine its χ^2–*curves* by allowing the parameter to vary within its assigned range while keeping all other parameters fixed at their values adopted by the appropriate lowest–χ^2_1 model. Of course, such curves not only allow us to identify a *formally best fitting model and parameter value* from their minima, but their specific shapes also provide a first idea of the *sensitivity* of the data to the variations of a particular parameter, whence a more quantitative estimate of the *permissible parameter range* can be obtained. For example, Fig. 3 illustrates how the two–dimensional (G,G-R) and the one–dimensional (G **or** G-R) observations for the field SA 54 are reproduced in different but mutually consistent ways by models calculated for variable local densities of the thick disk, n_1. The close coincidence of the minima near n_1 = 0.04 for all three χ^2–curves demonstrates that the observed data are internally consistent to a high degree, and that an optimized parameter value and associated permissible range can be reliably derived from the χ^2_1 estimate, if due account is taken of the χ^2–growth rates with changing n_1 exhibited by the one–dimensional χ^2_2– and χ^2_3–curves. This will be done below by applying an appropriate weighting scheme.

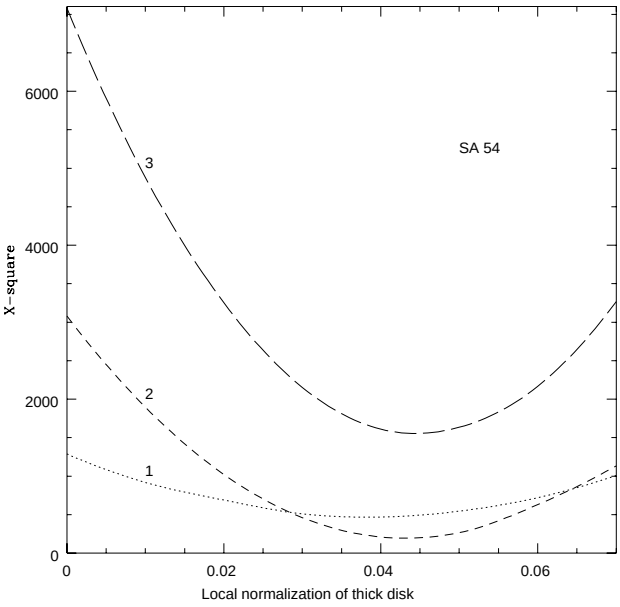

Fig. 3. χ^2_i–curves for the local density parameter, n_1, of the thick disk as measured by the *SA 54* field data. Labels indicate i.

The need for taking full advantage of the information contained in the *two–color* data is further illustrated in Fig. 4. Here, the three minima are dispersed over a larger range in n_1, indicating a somewhat lesser degree of internal consistency of the data for the field M67 – as opposed to the nearly ideal example shown for the field SA 54 in Fig. 3. On the other hand, with changing n_1 all the χ^2–growth rates are flatter in Fig. 4 than they are in Fig. 3, which shows that the *sensitivity* of the data to variations of the particular parameter n_1 is lower for the M67 field than for the higher–latitude field SA 54.

Thus, calculation of optimized parameter values is preferably based on the χ^2_1–curves, because these curves in turn are based on model fits to the *two–dimensional* $(G, G-R)$ *data*, and therefore provide stronger parameter constraints than each

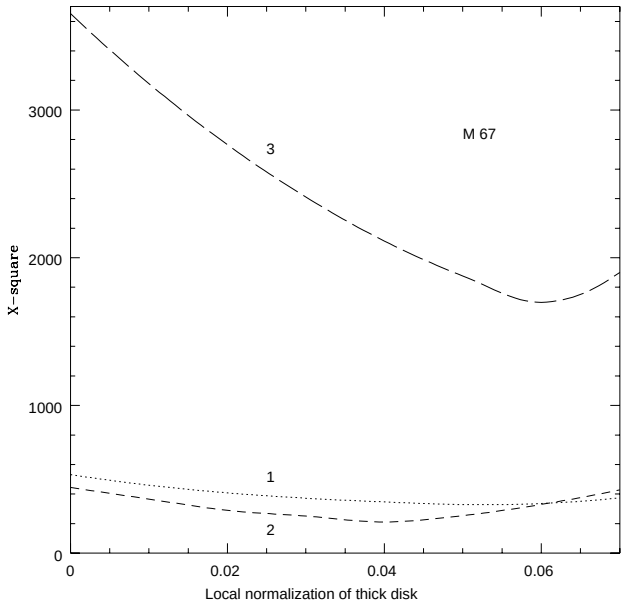

Fig. 4. χ_i^2–curves for the local density parameter, n_1, of the thick disk, as measured by the *M67* field data. Labels indicate i.

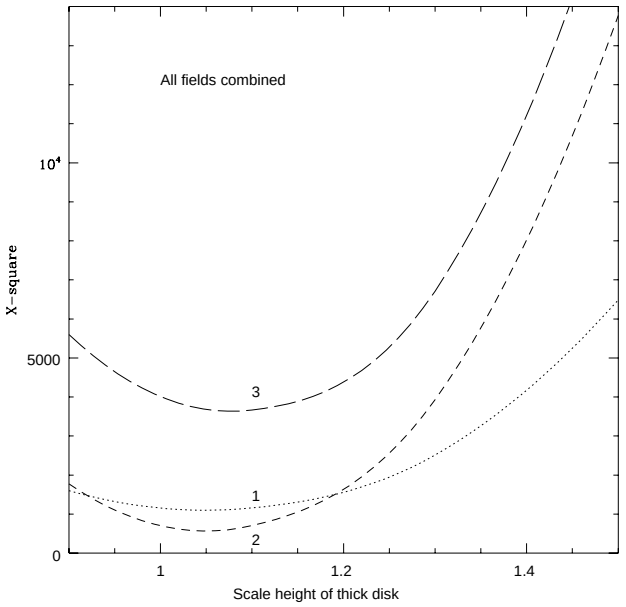

Fig. 6. Global χ_i^2–curves for the scale height of the thick disk, h_4. Labels indicate i.

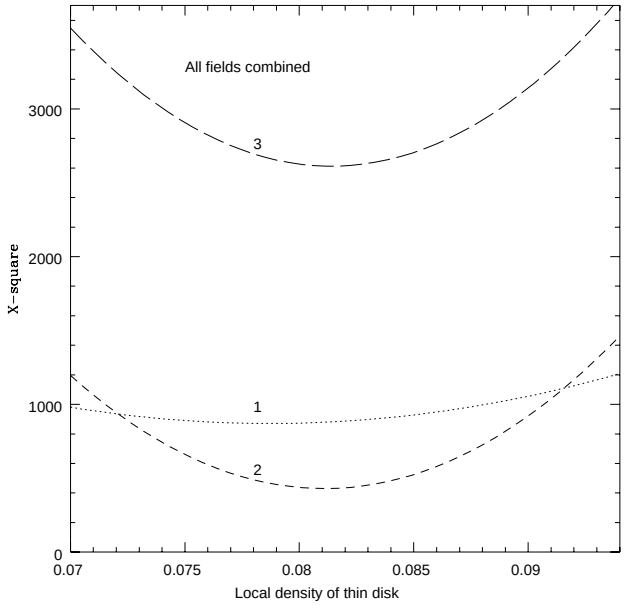

Fig. 5. Global χ_i^2–curves for the local density of the thin disk, n_0, in units of $stars/pc^3$. Labels indicate i.

of the two one–dimensional χ_2^2 and χ_3^2 estimates; but since the individual patterns exhibited by the different χ^2–curves actually depend sensitively on both the particular Galactic direction *and* the particular model parameter, this important source of information provided by the χ_2^2 and χ_3^2 estimates cannot be neglected in deriving optimized parameter values for both individual fields and the combined data in seven fields.

Examples of χ^2–curves for combined data in seven fields are illustrated for two parameters in Figs. 5 and 6.

In order to further explore the statistical significance of the $\chi_{1,min}^2$ model toward determining optimized parameter values and constraints, we proceed along the following line of reasoning: (1) for each parameter, by mathematical design its optimum value and constraints *must* be found from the *low*-χ_1^2 models; (2) the optimum value and constraints of a parameter are then given by the *frequency distribution* of its values occurring among the low-χ_1^2 models; (3) using this frequency distribution, the final *determination* follows by calculating a weighted average value and dispersion which account for the (particular) parameter's specific χ^2-curves.

In more detail, this procedure is realized in the following operational sequence (cf. also Pritchet 1983; Buser & Kaeser 1985):

4.2.2. Selection of acceptable models

We employ the parent population of *all* the models calculated in this work to define the sub-population of *acceptable* models by requiring that, for a model to be considered acceptable, it must satisfy the condition $\chi_1^2 \leq \chi_{1,max}^2 \leq \xi \cdot \chi_{1,min}^2$, where $1 < \xi \leq 1.5$ is an (as yet) arbitrary numerical factor that determines the maximum allowed χ_1^2–value of the acceptable model selection. We shall see below that, at least for the present preliminary analysis, a value of $\xi = 1.1$ as an *a priori* constraint on the goodness of fit appears to be reasonably justified by both the accuracy of available star count data in general *and* the sensitivities of the model predictions with parameter variations.

4.2.3. Frequency distributions

For discrete choices of ξ increasing with increments $\Delta\xi = 0.1$ between $\xi = 1.1$ and $\xi = 1.5$, we now construct the *frequency distributions* of parameter values by counting the number of acceptable models where a given parameter value occurs. Intuitively, for each choice of ξ, a larger number of models, i.e.,

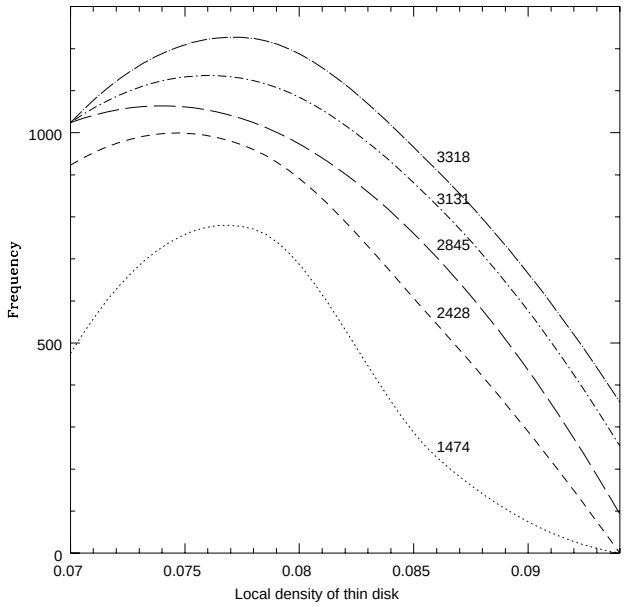

Fig. 7. Frequency distributions for the local density of the thin disk, n_0, derived from the combined survey of seven fields. The sequence of curves from bottom to top corresponds to growing values of ξ: labels indicate the number of models involved.

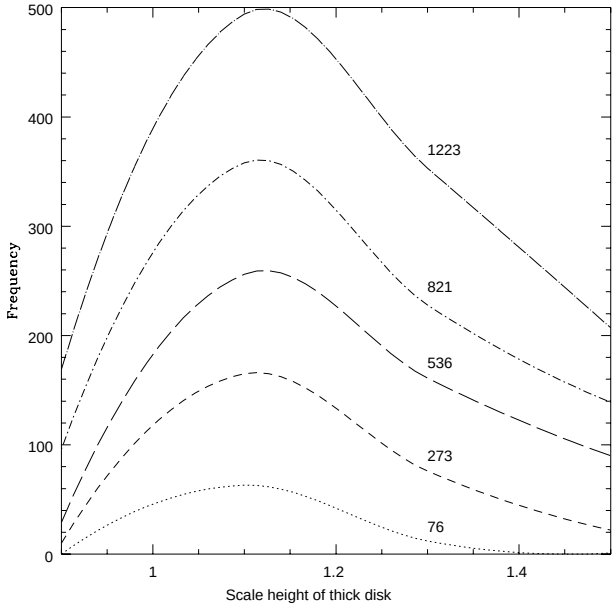

Fig. 8. Frequency distributions for the scale height of the thick disk, h_4, derived from the combined survey of seven fields. The sequence of curves from bottom to top corresponds to growing values of ξ: labels indicate the number of models involved.

a higher frequency of occurrence of a given parameter value, indicates a higher probability for this value to be true.

The idea behind this principle is the following. Because the large number (12) of parameters allow many models to reproduce the observed star counts and color distributions by chance, i.e., to provide low χ^2-scores even for unrealistic combinations of parameter values, the *truly* good models can be identified *via negationis* by arguing that a parameter value that *does not appear* among the low-χ^2 models *cannot* be the true one. Quantitatively, a slightly relaxed formulation of this criterion then leads one to investigate the above *frequency distributions* of parameter values among the whole sub-population of acceptable models defined in the previous step above.

Note that the calculations are performed on a sub-population of models drawn from a parent population which includes *all possible combinations of parameter values* ranging within their adopted variation limits. Therefore, the present selection of acceptable models not only includes models differing on account of the permissible variation of a particular parameter, but automatically also allows for both uncoupled and coupled variations of all other parameters. *A fortiori,* the same holds for the frequency distributions that are hence derived for each individual parameter. Thus, the subsequent determination of optimized parameter values and constraints does *not* suffer from selection bias due to the *neglect* of the effects of parameter coupling – which would be the case if, as usual, only the χ^2_1-curves were employed instead for this purpose.

The significance of the ξ-factor is illustrated in Figs. 7 and 8, which show that, with increasing ξ, increasing numbers of acceptable models exist for growing ranges of parameter values. However, the very existence and relative stability of pronounced peaks along with the similarities of the shapes of the successive distributions also suggest that reliable *optimized parameter values*, $\bar{p}$, may indeed be derived from the *representative* $\xi = 1.1$–selections of the (up to several hundred) *good models*, i.e., those which satisfy the condition $\chi^2_1 \leq \chi^2_{1,max} \leq 1.1 \cdot \chi^2_{1,min}$.

On the other hand, since in general, the associated dispersion $\sigma_{\bar{p}}$ shows a stronger dependence on ξ (as visualised by the increasing half–widths of the frequency distributions in Figs. 7 and 8), it may be more difficult to derive similarly reliable *constraints on* $\bar{p}$. Indeed, for this purpose the calculation of $\sigma_{\bar{p}}$ itself may reasonably be constrained *independently* by choosing ξ in such a way as to provide a maximum allowed $\chi^2_{1,max}$ which matches the *external* accuracy of the star count data.

Thus, for the purpose of the present paper, we have used 20% as a rough number for the external accuracy of available star count data, as judged from independent observations of several fields studied by different authors and techniques (Bahcall & Soneira 1984). As it turns out, this number is fairly well accommodated in the present calculations using $\chi^2_{1,max}$ implied by the $\xi = 1.1$–selection of models. In fact, most of our total predicted counts agree with the observations to within better than $\sim 30\%$ if $\xi \leq 1.2$ but get rapidly worse if $\xi > 1.2$.

4.2.4. Parameter coupling

As anticipated in the previous Subsect. 4.2.3, the present scheme has been explicitly designed to cope with the unavoidable presence of coupling among many parameters. Since each Galactic direction has its own pattern of sensitivities to the various parameter variations, it is important that the selection of good models invariably also include those for which parameter cou-

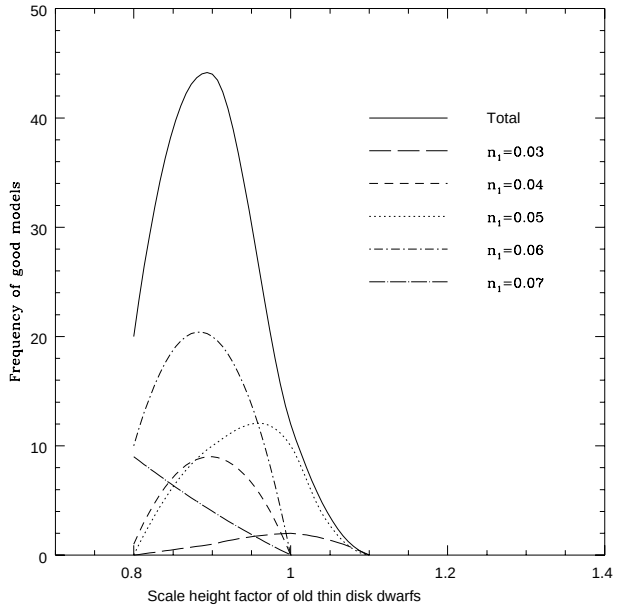

Fig. 9. Frequency distribution for old thin-disk dwarf scale height factor, h_1, among good models, illustrating the *presence* of parameter coupling with the local normalization of the thick disk, n_1 (labels in insert): for small/large values of n_1, the maximum of the frequency distribution preferentially occurs at large/small values of h_1, while the optimum value, h_1 = 0.9, is associated with intermediate values of n_1 – as indicated by the curve for the overall total. These results were derived from the combined survey of seven fields.

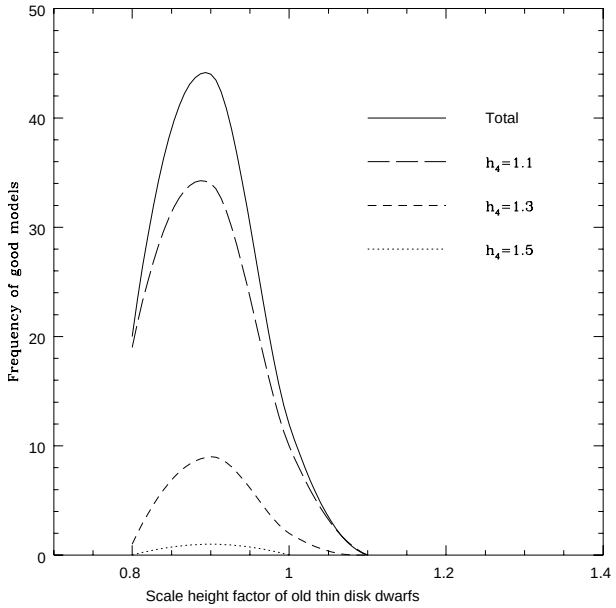

Fig. 10. Frequency distribution for old thin-disk dwarf scale height factor h_1 for the lowest–χ^2 models, illustrating the *absence* of parameter coupling with thick-disk scale height, h_4 (labels in insert): for all values of h_4, the frequency distributions are similar, having stable maxima at the same value of h_1 = 0.9. These results were derived from the combined survey of seven fields.

ples exist where allowed variation of the first parameter *happens* to compensate for the effect brought about by the (corresponding) allowed variation of a second parameter. This may lead to a frequency distribution of low–χ^2 models which is different from the corresponding univariate distribution (where only one parameter is allowed to vary) and, consequently, to different derived optimum parameter values and constraints.

Presence or absence of parameter coupling are illustrated in Figs. 9 and 10, respectively. In either case the ξ = 1.1–selection of good models leads to frequency distributions which are strongly peaked at thin–disk dwarf scale height factor h_1 = 0.9 and which are actually built from models covering large ranges of the local thick–disk density, $0.03 \leq n_1 \leq 0.07$ or the thick–disk scale height, $1.1 \leq h_4 \leq 1.5$, respectively.

4.2.5. Optimized parameter values

The statistical weight of a parameter value, $p(i)$, occurring in model i from the selection of good models is calculated taking into account this model's χ^2_2– and χ^2_3–estimates derived (above) from the *independent* fits of the model to the G– and G-R–data:

$$w_1(i) \;=\; \chi^2_{2,min}/\chi^2_2(i),$$
$$w_2(i) \;=\; \chi^2_{3,min}/\chi^2_3(i),$$

where $\chi^2_{2,min}$ and $\chi^2_{3,min}$ are calculated for *an individually or* **the** *globally best–fitting model*.

The *optimized parameter value,* $\bar{p}$, either for an individual field **or** for the combined G, G-R survey data in seven fields, is then computed from

$$\bar{p} \;=\; \sum_{i=1}^{n} p(i) \cdot w_1(i) \cdot w_2(i) / \sum_{i=1}^{n} w_1(i) \cdot w_2(i),$$

where n is the number of good models selected by the ξ = 1.1–criterion.

Figs. 11–13 provide representative illustrations of how such calculations reproduce the observed marginal distributions, $N(G)$, $N(G-R)$, or $N(U-G)$, for the fields Praesepe, SA 57, or M 101, respectively. In each figure, the observed histogram is compared with two model–generated distributions that are based on the optimized parameter values derived for *either* the particular individual field (dotted line) *or* the combined survey of seven fields (dashed line). While, of course, the individual model–fits are superior to the global fits *by definition*, the rather non–systematic and relatively weak differences between the two kinds – which are typical for all seven fields – clearly show that the survey data are *highly homogeneous* and that the structural parameters hence derived have a high probability of being *realistic*. This conclusion will be further supported by the following discussions of the metallicity structure derived from the three–color data.

4.2.6. Mean metallicities and metallicity gradients

Apart from deriving improved structural parameters and constraints, the principal goal of this project is to determine the

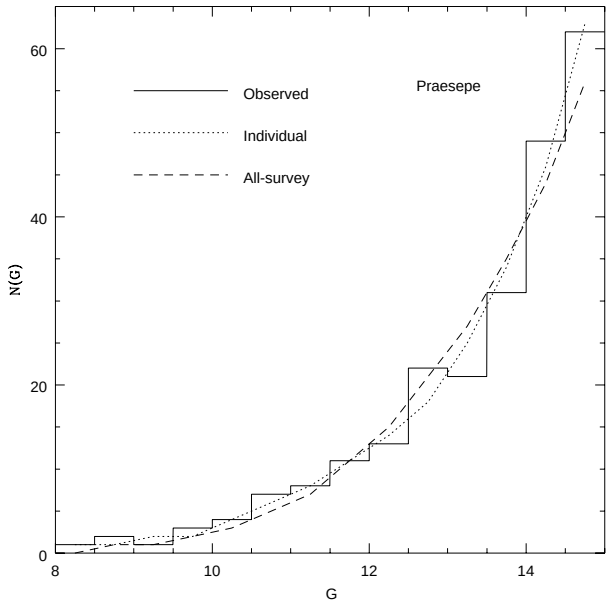

Fig. 11. Star counts in the *Praesepe* field. The observed histogram is compared with model predictions based on parameter values optimized for either this individual field (dotted line) or for the combined survey of seven fields (dashed line).

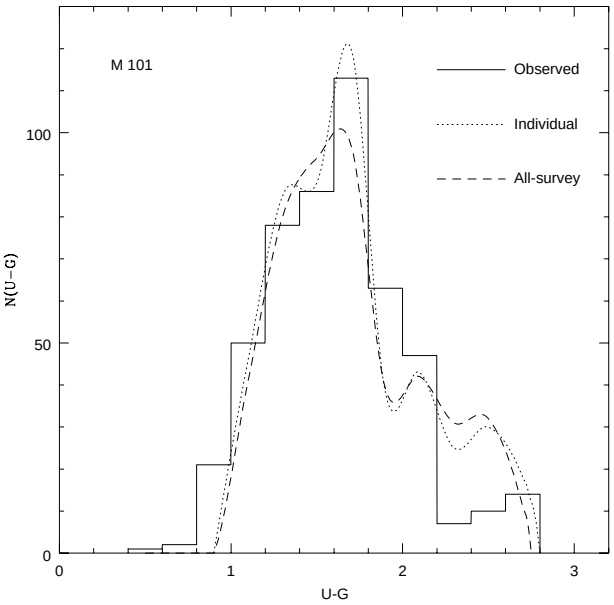

Fig. 13. $U-G$ color distribution in the field *M 101*. The observed histogram is compared with models based on parameter values optimized for either this individual field (dotted line) or for the combined survey of seven fields (dashed line).

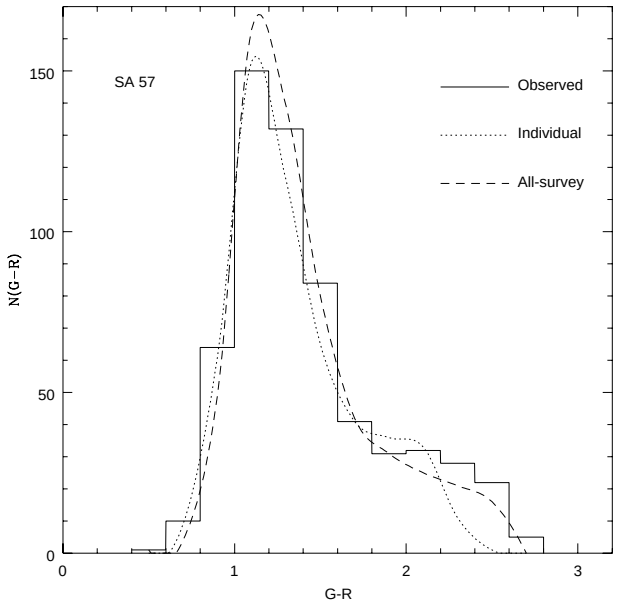

Fig. 12. $G-R$ color distribution in the field *SA 57*. The observed histogram is compared with models based on parameter values optimized for either this individual field (dotted line) or for the combined survey of seven fields (dashed line).

metallicity structure of the thick disk component. In fact, one important way of addressing the yet unsolved question concerning the *cosmogonic status of the thick disk* consists in assessing its large–scale metallicity distribution: is it spatially uniform or variable; if it is variable, is there or isn't there uniformity even in its variation, as the presence or absence of one (or several) metallicity gradient(s) might reveal?

As a first attempt at answering these important questions, the thick disk is modelled in either of two basic ways:

1. as a *chemically homogeneous* component whose stars all have the same $[M/H] = constant$. In order to derive the most probable value consistent with our survey data, a large number of models are calculated where the *constant* is allowed to range in the interval $[-0.5, -1.0]dex$; of course in this case, the adopted $[M/H]$ is identical with the *mean metallicity*, $\langle[M/H]\rangle$, of the thick disk component;
2. as a component whose chemical structure is characterizable by a *vertical metallicity gradient*, $\partial[M/H]/\partial z$, giving rise to a metallicity distribution with wider (and possibly also non–gaussian) dispersion about a field–specific "mean" metallicity; again, in order to derive the most probable values consistent with our survey data, a large number of models are calculated where $\partial[M/H]/\partial z$ is allowed to range in the interval $[0.0, -0.5]dex/kpc$.

Since the metallicity structure of the *thin disk* has been better known from spectroscopic investigations, calculations are run for only a few representative values of its mean metallicity and gradient to ascertain consistency with the canonical literature. As we shall see, the present data do not allow us to determine whether or not a metallicity gradient exists in the field *halo*. Thus, calculations are made for a few discrete values of the halo's mean metallicity only in order to ascertain consistency with canonical results from the literature.

Comparison of model calculations with observations is now performed using both two–dimensional distributions, $N(G, G-R)$ and $N(G, U-G)$, to reinforce the metallicity–sensitivity provided by the additional $U-G$ data. Thus, for each model

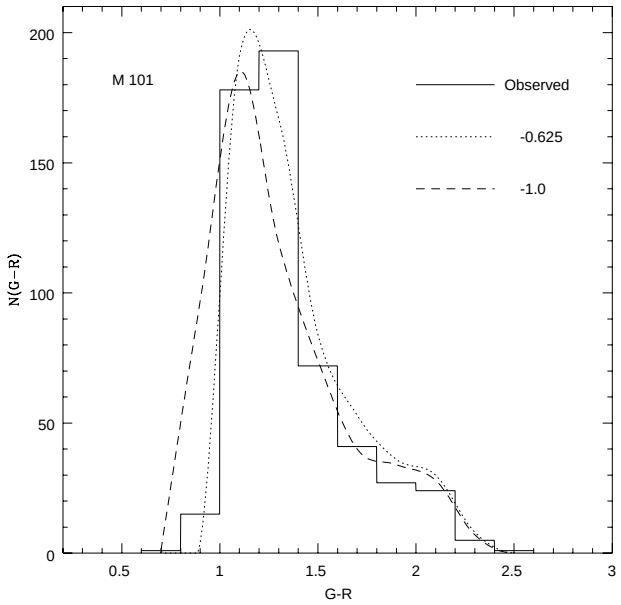

Fig. 14. $G-R$ color distribution in the field *M101*. The observed histogram is compared with models that differ only in the mean metallicity adopted for the thick disk component: $\langle[M/H]\rangle = -0.625$ (dotted line) and $\langle[M/H]\rangle = -1.00$ (dashed line).

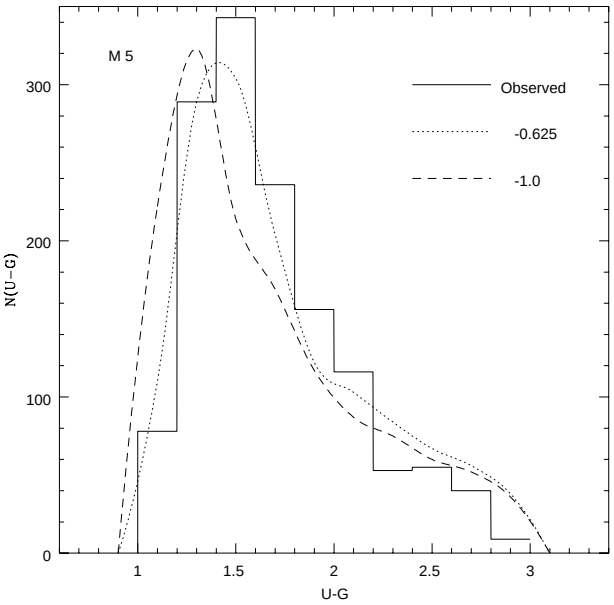

Fig. 15. $U-G$ color distribution in the field *M5*. The observed histogram is compared with models that differ only in the mean metallicity adopted for the thick disk component: $\langle[M/H]\rangle = -0.625$ (dotted line) and $\langle[M/H]\rangle = -1.00$ (dashed line).

and field $k = 1, \ldots, 7$ we calculate

$$\chi^2_{4,k} = \frac{1}{2} \cdot \Big(\sum_{bins} [N_{obs}(G, G-R) - N_{mod}(G, G-R)]^2 + \sum_{bins} [N_{obs}(G, U-G) - N_{mod}(G, U-G)]^2 \Big),$$

and individually or globally best–fitting values for $\langle[M/H]\rangle$ or $\partial[M/H]/\partial z$ are derived following a similar statistical analysis as before.

The sensitivities of the predicted color distributions to changes of the mean metallicity in the model of the thick disk component are illustrated in Figs. 14 and 15. Note that both the predicted blue edges and peaks of the distributions are significantly different in either color for an assumed difference of order $0.3dex$ in the mean metallicity of the thick disk. Although the high metallicity sensitivity persists into the red wings of the distributions, the somewhat poorer quality of the model fits is due to the increasing uncertainty of the color–magnitude and two–color calibrations for the reddest stars (Buser & Fenkart 1990, Buser & Kurucz 1992). However, a special effort is being made to improve the temperature and metallicity calibrations of the stellar library underlying the synthetic photometry employed in this work (Lejeune et al. 1997a,b), which will also improve our treatment of the coolest stars in the impending analysis of the full–survey data in 14 fields.

For the present first–half sample of the survey, typical results obtained for the mean metallicity of the thick disk component are illustrated in Figs. 16 and 17, which show the χ^2–curves derived from the data in the South Galactic Pole field SA 141 and from the combined data in seven fields. Note that these results are based on the assumption that the thick disk has uniform mean metallicity throughout its range, with a (gaussian) dispersion, $\sigma_{\langle[M/H]\rangle} \sim 0.2dex$, corresponding to the dispersions of the color–magnitude relations adopted in converting the luminosity function appropriate to the given mean metallicity from the $M_V, B-V, U-B$ system to the $M_G, G-R, U-G$ system. We shall see below that while the good models in Fig. 17 suggest that the thick disk has $\langle[M/H]\rangle \sim -0.6 \pm 0.25dex$, the somewhat more detailed model including a metallicity gradient indicates that the *true dispersion* may be significantly larger.

5. Results and discussion

Results of the preceding analyses are summarized in Tables 3 and 4, for both the individual fields and the combined survey of seven fields. In the following subsections, the optimized structural parameters found for the density models of all four Galactic components and the metallicity structures of the thin disk and halo are discussed in turn, before we finally present our preliminary conclusions on the metallicity structure of the thick disk component.

5.1. Optimized values and constraints: primary parameters

The determination of optimized parameter values and constraints is based on the analysis of the $\chi^2 \leq 1.1 \cdot \chi^2_{min}$–selection from a large range of models, as described in Sect. 4.2. Due to the systematic coverage of high latitudes, we expect the survey data to be particularly suitable for measuring the scale heights of the old thin and thick disks, and for providing reliable extrapolations of the thick-disk and halo densities to the local

Table 3. Optimized parameter values

	Primary parameters, $\bar{p}_k$						Secondary parameters, $\bar{p}_k$					
	Thin disk			Thick disk		Halo	Thin disk			Thick disk	Halo	
Field, k	d_1	h_1	h_3	n_1	h_4	n_2	n_0	h_2	d_2	d_3	R_{eff}	κ_0
1	4.95	1.19	0.15	0.068	1.05	0.0020	0.094	0.22	3.76	3.89	2.71	0.85
2	3.98	0.86	0.22	0.065	0.95	0.0003	0.081	0.24	3.75	4.28	2.70	0.85
3	4.03	1.02	0.19	0.052	0.96	0.0014	0.082	0.22	3.70	4.16	2.69	0.85
4	3.93	0.81	0.18	0.040	1.13	0.0010	0.075	0.25	3.75	4.25	2.69	0.84
5	3.99	0.80	0.19	0.054	1.02	0.0011	0.079	0.24	3.75	4.25	2.63	0.79
6	4.02	0.97	0.15	0.021	1.11	0.0023	0.081	0.26	3.75	4.25	2.67	0.80
7	3.96	0.97	0.15	0.062	1.12	0.0003	0.077	0.24	3.75	4.35	2.70	0.84
$\bar{p}_{1-7}$	4.01	0.90	0.17	0.054	1.15	0.0005	0.078	0.25	3.75	4.25	2.69	0.84
$\sigma_{\bar{p}_{1-7}}$	1.0	0.1	0.03	0.015	0.15	0.0003	0.005	0.05	–	1.0	–	–

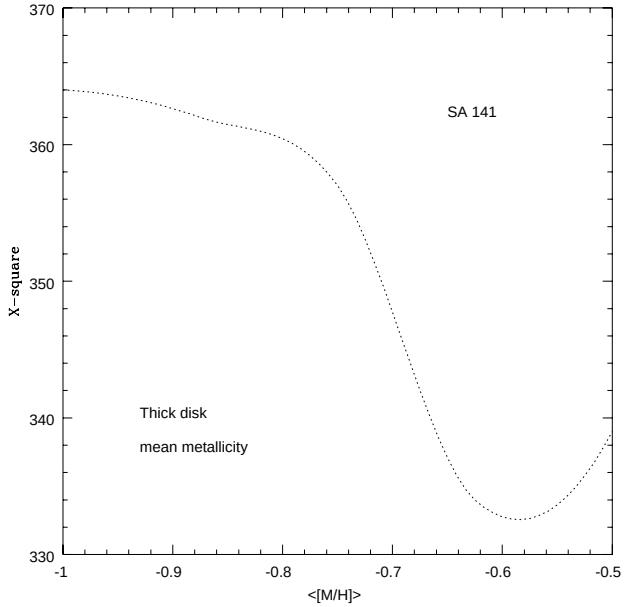

Fig. 16. χ^2–curve for the thick-disk mean metallicity derived in the South Galactic Pole field *SA 141*. The sharp minimum suggests that in this field, $\langle[M/H]\rangle \sim -0.6dex$.

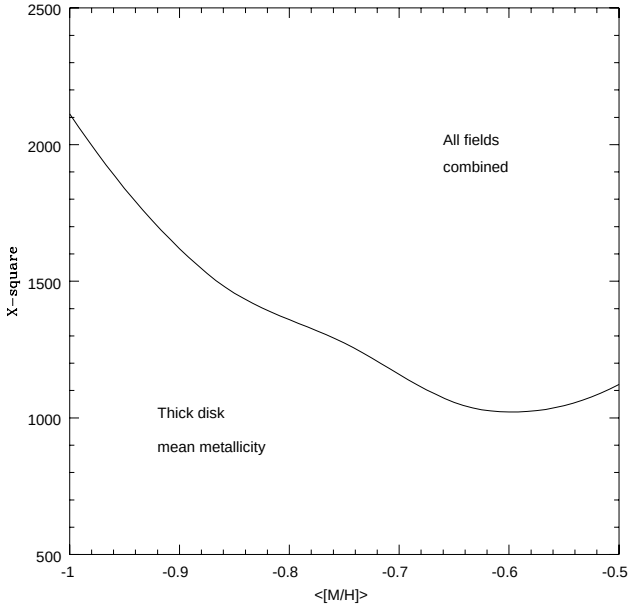

Fig. 17. χ^2–curve for the thick-disk mean metallicity derived from the all–survey data in seven fields. The minimum suggests that globally, the data are consistent with a model that assumes a thick disk with homogeneous metallicity $\langle[M/H]\rangle \sim -0.6dex$.

volume near the sun. For all the individual fields as well as for the combined survey of seven fields, the χ^2–curves for these parameters do indeed show the most pronounced minima, with growth rates increasing to several times χ^2_{min}, fully vindicating the above expectations. Thus, the most important conclusion to be drawn from the results given in the bottom lines of Table 3 is that, apart from its thin disk with canonical scale height $h_1 = (0.90 \pm 0.1) \cdot 325pc \simeq 290 \pm 30pc$, *the Milky Way Galaxy has a thick disk with a local density of* $n_1 = 5.4 \pm 1.5\%$ *relative to the thin disk and scale height* $h_4 = 1.15 \pm 0.15kpc$, *and only a weak halo with local density* $n_2 = 0.0005 \pm 0.0003$ *relative to the thin disk.* The thick disk portrayed by the above results appears to be a more substantial component than originally suggested by Gilmore and Reid (1983) and by Fenkart (1989a–d), but fits well with the picture emerging from the more recent studies discussed by Majewski (1993).

On the other hand, the present survey data are rather less sensitive to the two remaining primary parameters, the scale length of the old thin disk, d_1, and the scale height of the young thin-disk dwarfs, h_3. Over the full variation ranges explored for these parameters, the χ^2–curves have amplitudes which are of order 25% or less only above their χ^2_{min}, and the corresponding frequency distributions for the good models are rather flat. Therefore, although optimized mean values could be derived with surprisingly little scatter from field to field, the actual constraints imposed on these values from the combined survey data are not very strong.

5.2. Consistency with external data: secondary parameters

A gratifying result of the present analysis is that, upon determination of optimized values and constraints for the *primary parameters*, the *secondary parameter values* – which are left to freely float for final adjustment only *after* the primary parameters –, come out in close agreement with external data and

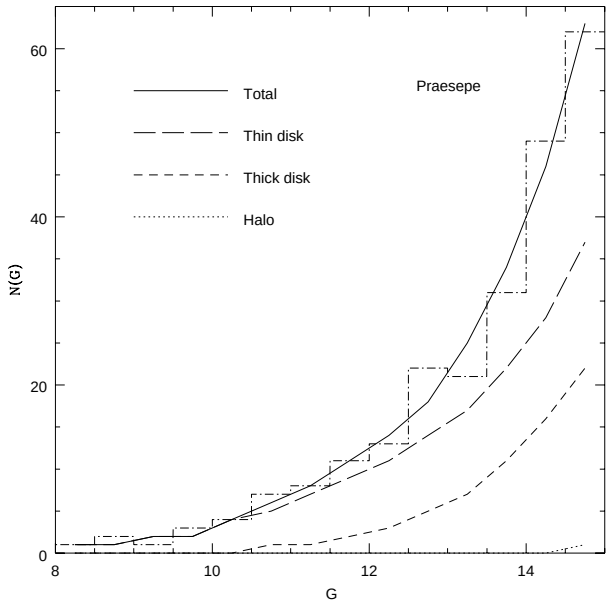

Fig. 18. Star counts N(G) in the *Praesepe* field, comparing the observed histogram with the predicted total built up by the contributions from the individual components. The thin disk dominates down to the magnitude limit at G = 15. Compare with Fig. 11.

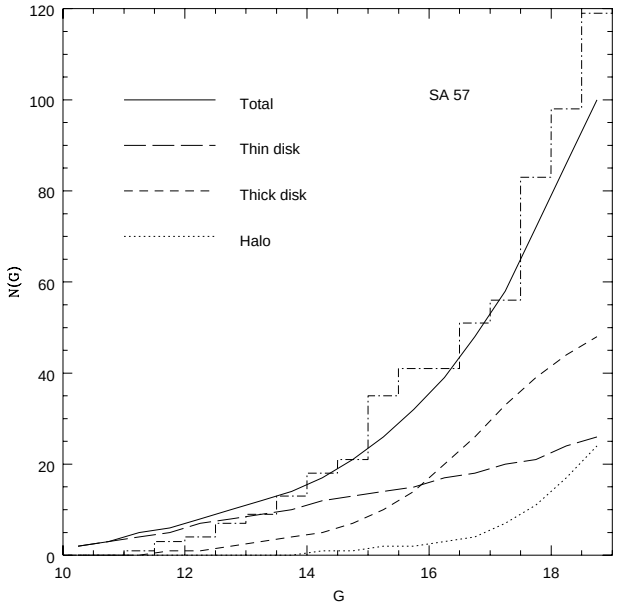

Fig. 19. Star counts N(G) in the field *SA 57*, comparing the observed histogram with the predicted total built up by the contributions from the individual components. The thin disk dominates down to G = 16 but is overtaken by the thick disk and the halo at fainter magnitudes.

constraints. For example, although the local density of the thin-disk dwarfs has been left to float in the range between 0.07 and 0.10 $stars/pc^3$, the final optimized result turns out to be n_0 = 0.078 $\pm$ 0.005 $stars/pc^3$, which is almost identical to the n_0 = 0.080 $stars/pc^3$ derived from the Gliese–Wielen luminosity function, if due account is taken of the frequency of binary and multiple stars that remain unresolved at the typical

Table 4. Mean metallicity and gradient of thick disk

	Thick disk metallicity model		
	No gradient	Including gradient	
Field	$\langle[M/H]\rangle$	$\partial[M/H]/\partial z$	$\langle[M/H]\rangle$
1	-0.77	-0.20	-0.81
2	-0.64	-0.04	-0.60
3	-0.69	-0.20	-0.78
4	-0.59	-0.05	-0.52
5	-0.59	-0.03	-0.49
6	-0.58	-0.15	-0.76
7	-0.59	-0.03	-0.54
1-7	-0.64	-0.10	-0.58
$\sigma_{\langle[M/H]\rangle}$	$\pm$0.25		+0.30,-0.50

distances and the low–angular resolution of the Basel Palomar–Schmidt field survey (Buser & Kaeser 1985).

On the other hand, due to the relatively limited survey range of the thin disk and the steep decline of the luminosity function toward bright stars, the present survey data are rather insensitive to the density parameters of the brighter dwarfs of the young thin disk and the giants of the old thin disk. Therefore, the mean values for these parameters (e.g., d_2, h_3) are not, in general, strongly constrained by the χ^2–curves and their associated frequency distributions. However, since the systematic coverage of many Galactic directions also provides adequate coverage of the different sensitivity ranges for all such low–sensitivity parameters – which also include the scale length of the thick disk, d_3, and the halo parameters $R_{\rm eff}$ and κ_0 –, the mean values derived from the data aggregate in seven fields are evidently derived consistent with independent investigations (Majewski 1993).

Similarly, even though the present survey was *not* specifically designed for determining the chemical structure of the *thin disk*, the data provide strong enough samplings of this component for a significant measurement of its *vertical metallicity gradient* – and "mean" metallicity. This is due to the fact that first, there is a large enough number (5 out of 7) of directions where the thin disk dominates the star counts down to the limiting magnitudes of the survey (cf. Figs. 18 and 19), and second because the colors are sufficiently metallicity sensitive to warrant significant mapping of the metallicity effect (Figs. 14 and 15).

Thus, the "mean" metallicity suggested by the minimum of the global χ^2–curve in Fig. 20 is fully consistent with the *thin disk* having mean metallicity $\langle[M/H]\rangle \sim 0.0$ dex in the very local volume, but which, due to a gradient $\partial[M/H]/\partial z \sim -0.6$ dex/kpc, decreases by a factor of ~ 2 in the more distant thin–disk volumes sampled by the present survey. These results are in good agreement with those obtained from photoelectric photometry and spectroscopy for smaller samples of G–K giants and F–G dwarfs by Yoss et al. (1987) and by Trefzger et al. (1995).

On the other hand, because the present survey does not penetrate to very faint magnitudes, the field *halo* is not well sampled out to its farthest reaches. Therefore, while a metallicity gradient

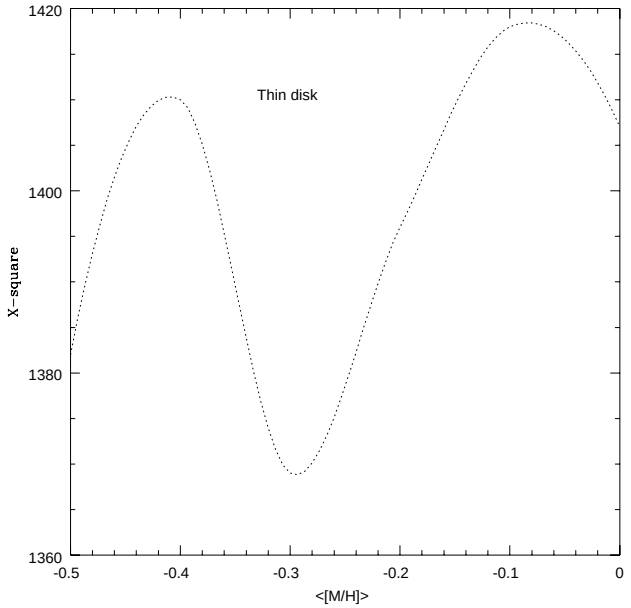

Fig. 20. χ^2–curve for the thin-disk mean metallicity derived from the all–survey data in seven fields. Although only weakly pronounced, the minimum near $\langle[M/H]\rangle \sim -0.3$ dex goes along with a vertical metallicity gradient $\partial[M/H]/\partial z = -0.6$ dex/kpc, which demonstrates that the present data and results are consistent with the canonical knowledge of this component.

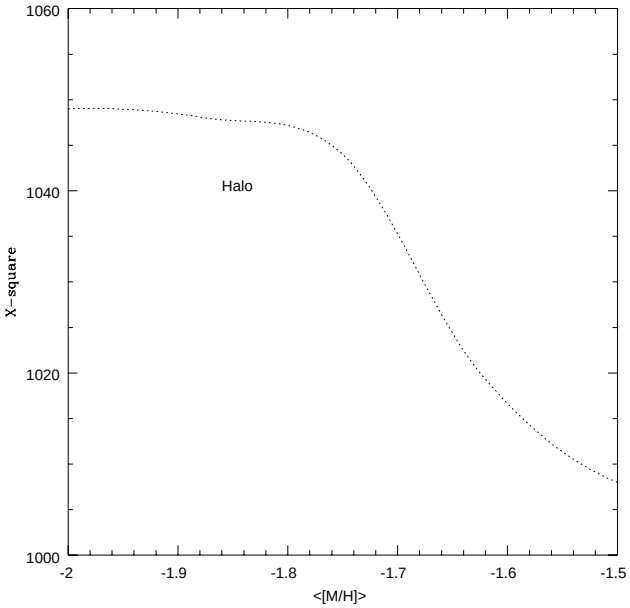

Fig. 21. χ^2–curve for the halo mean metallicity derived from the all–survey data in seven fields. The curve suggests that the minimum occurs near $\langle[M/H]\rangle \geq\sim -1.5$ dex, which is clearly different from the value (-1.75 dex) adopted initially.

for the halo could not be derived reliably, the mean metallicity, $\langle[M/H]\rangle \geq\sim -1.5$ dex, indicated by the global χ^2–curve in Fig. 21, is again consistent with canonical values.

5.3. Preliminary constraints: metallicity structure of thick disk

Table 4 summarizes the metallicity structure of the thick disk component that we find from the present (preliminary) analysis. As anticipated in 4.2.6, these results are derived assuming two different basic models: (1) for the chemically homogeneous model, we calculate a mean metallicity $\langle[M/H]\rangle = -0.64$ dex with dispersion $\sigma_{\langle[M/H]\rangle} = \sqrt{\sigma_{int}^2 + \sigma_{ext}^2} = 0.25$ dex, where $\sigma_{int} = 0.2$ dex is the dispersion intrinsic to the adopted color–magnitude and color–color relations and $\sigma_{ext} = 0.15$ dex is the dispersion derived from the χ^2–curves and frequency distributions of the good models; (2) for the model including chemical gradients, the mean metallicities in each field are calculated from the best–fitting gradient solution and averaging all the individual stellar metallicities summed over the successive volumes. Interestingly, this model gives a marginally higher "mean" metallicity, $\langle[M/H]\rangle = -0.58$ dex, but with a somewhat larger dispersion $\sigma_{\langle[M/H]\rangle} \sim 0.4$ dex which is slightly skewed toward lower metallicities. Clearly, the stronger derived gradients in fields 1, 3, and 6 of Table 4 predict lower metallicities for larger distances and, hence, for the implied larger count contributions, leading to lower "mean" metallicities for these fields as well.

Even though the results of Table 4 do not yet provide a definitive answer to the question of whether or not (a) gradient(s) exist(s) in the thick disk – because the numerical data are still consistent with either of the above model assumptions on the two–sigma level –, what they seem to indicate however is that chemical *inhomogeneities* are likely present in this component which give rise to a rather larger metallicity spread than anticipated initially. We expect that a more refined and comprehensive analysis of the full–survey data in 14 fields will allow us to considerably sharpen the present picture.

6. Summary and outlook

In the present paper, we have developped and tested a comprehensive computer algorithm for the statistical analysis of three–color star count data. This algorithm has been applied to the first-half sample of the new catalog of homogeneous RGU data in seven fields of the Basel high–latitude survey in order to determine optimized parameter values and constraints for models of the density, luminosity, and metallicity distributions of the Galactic field star populations. While our first results confirm that the new data indeed allow us to derive density and metallicity structures which are, by and large, consistent with currently accepted values for all major stellar components of the Galaxy, they also indicate that, due to their high statistical weight, the present new survey data may also carry the potential for deriving the *large–scale properties of the thick disk* with higher confidence than before. Thus, the evidence for the *thick disk component* will be exposed in greater detail in Paper II of this series, in particular by expanding our studies of the luminosity function and the metallicity distribution.

Beginning with Paper V, we shall provide *more definitive results* based on the analysis of the *complete survey data in*

all 14 Basel fields, and taking advantage of further *extended and improved RGU system calibrations* expected from the new synthetic photometry data base constructed by Lejeune et al. (1997a,b). This will, finally, also allow us to assess the significance of the results derived from the present project in terms of comprehensive comparisons with independent studies of the Galactic density and/or chemical abundance distributions from both multiple–field (e.g., Gould et al. 1993, Ojha et al. 1994a,b, Robin et al. 1996, Soubiran 1993) and unidirectional high-latitude surveys, e.g., in SA 57 [North Galactic Pole] (Chen 1997, Reid & Majewski 1993, Spagna et al. 1996), SA 94 (Friel & Cudworth 1986), M5 (Perrin et al. 1995), and SA 54 (Yamagata & Yoshii 1992).

Acknowledgements. We would like to thank the referee for constructive comments that have led to improvements of this paper. This work was supported by the Swiss National Science Foundation.

References

Arimoto N., 1986, A&A, 164, 260
Bahcall J.N., 1986, ARA&A, 24, 577
Bahcall J.N., Soneira R.M., 1984, ApJS, 55, 67
Bahcall J.N., Ratnatunga K.U., Buser R., Fenkart R.P., Spaenhauer A., 1985, ApJ, 299, 616
Becker W., 1965, Zs.f.Astrophys., 62, 54
Becker W., 1980, A&A, 87, 80
Becker W., Fenkart R., 1976, Photometric Catalogue for Stars in Selected Areas and Other Fields in the RGU–System, Vol. I, Astron. Inst. Univ. Basel
Becker W., Fenkart R., Schaltenbrand R., Wagner R., Yilmaz F., 1976, Photometric Catalogue for Stars in Selected Areas and Other Fields in the RGU–System, Vol. II, Astron. Inst. Univ. Basel
Becker W., Steinlin U., Wiedemann D., 1978, Photometric Catalogue for Stars in Selected Areas and Other Fields in the RGU–System, Vol. V, Astron. Inst. Univ. Basel
Becker W., Fenkart R., Karaali S., del Rio G., 1988, Photometric Catalogue for Stars in Selected Areas and Other Fields in the RGU–System, Vol. XI, Astron. Inst. Univ. Basel
Becker W., Fenkart R.P., Boydag S., Kandemir G., Karaali S., Spaenhauer A., Tammann G., Topaktas L., 1989, Photometric Catalogue for Stars in Selected Areas and Other Fields in the RGU–System, Vol. XII, Astron. Inst. Univ. Basel
Blitz L., Teuben P. (eds.), 1996, Unsolved Problems of the Milky Way, IAU Symp. 169, Dordrecht: Kluwer
Burstein D., Heiles C., 1982, AJ, 87, 1165
Buser R., 1978, A&A, 62, 425
Buser R., 1988, in Impacts des surveys du visible sur notre connaissance de la Galaxie, eds. A. Fresneau & M. Hamm, Comptes Rendus sur les Journées de Strasbourg, 9ème Réunion, Obs. de Strasbourg, p. 15
Buser R., Fenkart R.P., 1990, A&A, 239, 243
Buser R., Kaeser U., 1985, A&A, 145, 1
Buser R., Kurucz R., 1992, A&A, 264, 557
Buser R., Rong J.X., 1995, Baltic Astron., 4, 1
Buser R., Karaali S., Topaktas L., Karatas Y., Rong J.X., 1997a, A&AS (Paper III, to be submitted)
Buser R., Karaali S., Topaktas L., Rong J.X., 1997b, A&AS (Paper IV, in preparation)
Buser R., Lejeune Th., Güngör S., Rong J.X., 1997c, A&A (in preparation)
Carney B.W., 1979, ApJ, 233, 211
Chen B., 1997, AJ, 113, 311
Fenkart R.P., 1989a, A&AS, 78, 217
Fenkart R.P., 1989b, A&AS, 79, 51
Fenkart R.P., 1989c, A&AS, 80, 89
Fenkart R.P., 1989d, A&AS, 81, 187
FitzGerald M.P., 1970, A&A, 4, 234
Friel E.D., Cudworth K.M., 1986, AJ, 91, 293
Gilmore G., Reid N., 1983, MNRAS, 202, 1025
Gilmore G., King I.R., van der Kruit P., 1990, The Milky Way as a Galaxy, eds. R. Buser & I.R. King, Saas–Fee Advanced Course 19, Mill Valley: University Science Books
Gliese W., 1969, Veröff. Astron. Recheninst. Heidelberg, No. 22
Gliese W., 1982, A&AS, 47, 471
Gould A., Bahcall J.N., Maoz D., 1993, ApJS, 88, 53
Güngör S., 1996, Ph.D. thesis, Istanbul Univ.
Jahreiss H., Gliese W., 1989, in Star Catalogues: A Centennial Tribute to A.N. Vyssotsky, eds. A.G. Davis Philip & Arthur R. Upgren, Contr. Van Vleck Obs. No. 8, Schenectady, N.Y.: L. Davis Press,, p. 11
Johnson H.L., 1966, ARA&A, 4, 193
Lejeune Th., Cuisinier F., Buser R., 1997a, A&AS, 125, 229
Lejeune Th., Cuisinier F., Buser R., 1997b, A&AS (in press)
Majewski S.R., 1993, ARA&A, 31, 575
Neckel H., 1975, A&A, 42, 379
Ojha D.K., Bienaymé O., Robin A.C., Mohan V., 1994a, A&A, 284, 810
Ojha D.K., Bienaymé O., Robin A.C., Mohan V., 1994b, A&A, 290, 771
Perrin M.-N., Friel E.D., Bienaymé O., Cayrel R., Barbuy B., Boulon J., 1995, A&A, 298, 107
Pilachowski C.A., 1984, ApJ, 281, 614
Pritchet C., 1983, AJ, 88, 1476
Reid N., Gilmore G., 1982, MNRAS, 201, 73
Reid N., Majewski S.R., 1993, ApJ, 409, 635
Robin A.C., Haywood M., Crézé M., Ojha D.K., Bienaymé O., 1996, A&A, 305, 125
Sandage A., 1982, ApJ, 252, 553
Schmidt-Kaler Th., 1965, in Landolt-Börnstein, Neue Serie, Gruppe VI, Bd. I, ed. H.H. Voigt, Springer, Berlin Heidelberg New York, p. 298
Schmidt-Kaler Th., 1982, in Landolt-Börnstein, Neue Serie, Gruppe VI, Bd. 2b, eds. K. Schaifers, H.H. Voigt, Springer, Berlin Heidelberg New York, p. 14
Soubiran C., 1993, A&A, 274, 181
Spagna A., Lattanzi M.G., Lasker B.M., McLean B.J., Massone G., Lanteri L., 1996, A&A, 311, 758
Trefzger Ch.F., Pel J.W., Gabi S., 1995, A&A, 304, 381
Wielen R., Jahreiss H., Krüger R., 1983, in The Nearby Stars and the Stellar Luminosity Function, eds. A.G. Davis Philip & A.R. Upgren, IAU Coll. 76, Schenectady, N.Y.: L. Davis Press, p. 163
Yamagata T., Yoshii Y., 1992, AJ, 103, 117
Yoshii Y., Ishida K, Stobie R.S., 1987, AJ, 93, 323
Yoss K.M., Neese C.L., Hartkopf W.I., 1987, AJ, 94, 1600

This article was processed by the author using Springer-Verlag LaTeX A&A style file *L-AA* version 3.